RESEARCH ARTICLE | MAY 12 2023

### Triple Langmuir probe calibration in TOMAS ECRH plasma

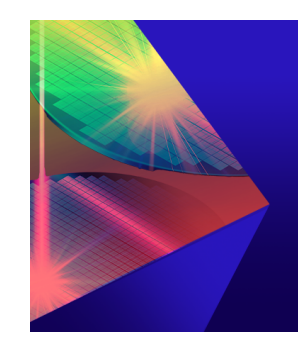
J. Buermans 🗷 🗓 ; K. Crombé 🗓 ; L. Dittrich 🗓 ; A. Goriaev 🗓 ; Y. Kovtun 🗓 ; D. López-Rodríguez 🗓 ; S. Möller 🗓 ; P. Petersson 🗓 ; M. Verstraeten 🗓



AIP Advances 13, 055125 (2023) https://doi.org/10.1063/5.0146388







## **AIP Advances**

Special Topic: Novel Applications of Focused Ion Beams — Beyond Milling

**Submit Today** 





# Triple Langmuir probe calibration in TOMAS ECRH plasma

Cite as: AIP Advances 13, 055125 (2023); doi: 10.1063/5.0146388

Submitted: 20 February 2023 • Accepted: 3 May 2023 •

Published Online: 12 May 2023







#### **AFFILIATIONS**

- <sup>1</sup>Laboratory for Plasma Physics LPP-ERM/KMS, Brussels, Belgium
- <sup>2</sup>Department of Applied Physics, Ghent University, Ghent, Belgium
- <sup>3</sup> Fusion Plasma Physics, KTH Royal Institute of Technology, Stockholm, Sweden
- Institute of Plasma Physics, NSC KIPT, Kharkov, Ukraine
- <sup>5</sup>Institute for Energy and Climate Research, Forschungszentrum Jülich GmbH, Jülich, Germany

a) Author to whom correspondence should be addressed: Johan. Buermans@ugent.be

#### **ABSTRACT**

In the TOMAS device, a triple Langmuir probe is used to measure the electron temperature and density. The accuracy of this measurement depends on correct determination of the effective collecting area of the probe, which depends on complex plasma transport processes. The probe can be calibrated by electron cyclotron resonance heating experiments using the cut-off density of the ordinary wave (O-wave). This threshold only depends on the frequency of the injected wave, and the occurrence of this phenomenon is clearly visible in the temperature evolution. The value of density is consequently known at this point and can be used to calibrate the density measurements of the triple Langmuir probe.

© 2023 Author(s). All article content, except where otherwise noted, is licensed under a Creative Commons Attribution (CC BY) license (http://creativecommons.org/licenses/by/4.0/). https://doi.org/10.1063/5.0146388

#### I. INTRODUCTION

Since the beginning of fusion research, Langmuir probes have played an important role in measuring the density and temperature in a plasma. It provides the input for plasma control and machine protection and more insights into the physics behind it. A good knowledge of the electron density and temperature is therefore necessary. The operation of a triple probe allows determining instantaneous values of these plasma parameters. Only a simple measuring circuit is required, and processing of the data seems straightforward.

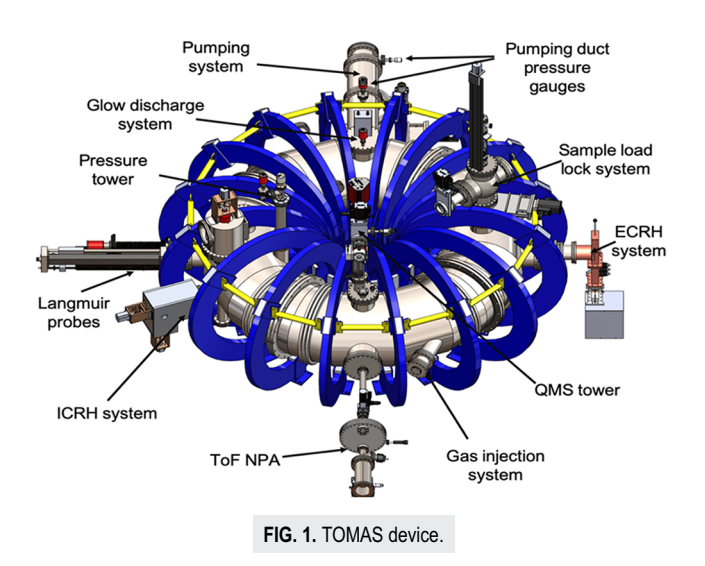
In contrast to the ease of use, interpreting the probe measurements in a correct way still remains a challenging problem. Several phenomena influence these measurements, including the variation in the ion saturation current,<sup>2</sup> the orientation of the magnetic field,<sup>3</sup> and the probe sheath expansion.<sup>4</sup> A means to calibrate the probe is needed to increase the accuracy and to refine the results.

The triple probe in the TOMAS device is calibrated by Electron Cyclotron Resonance Heating (ECRH) experiments using the

cut-off density of the ordinary wave (O-wave) as a reference. To explain how this calibration is performed, we first need to clarify how probe measurements are performed and processed. Thereafter, we need to explain how the wave properties in an ECRH plasma allow identifying a reference for density measurements. Combining these two principles in a series of experiments will allow us to calibrate the density measurements of the Langmuir probe.

#### II. THE TOMAS DEVICE

The TOMAS device (Fig. 1) is a TOroidally MAgnetized System (TOMAS), which is operated at FZ-Jülich. It is a facility designed to study plasma production, wall conditioning, and plasma–surface interaction studies. The metallic vessel has a major radius  $R=0.78\ m,$  a minor radius  $a=0.26\ m,$  and a plasma volume of  $1.1\ m^3.$  The variable toroidal magnetic field is created by 16 copper coils and can reach a maximum value of 125 mT on the torus axis, which equals a coil current of 2.2 kA.



The TOMAS device has several systems for plasma production: Glow Discharge Cleaning (GDC), Electron Cyclotron Resonance Heating (ECRH), and Ion Cyclotron Resonance Heating (ICRH). A magnetron with a frequency f = 2.45 GHz is used as the microwave source and can inject 0.7–6.0 kW of power. The matching is performed using a 3-stub tuner and an adjustable short. The reflected power level is measured using a zero-bias Schottky diode. A 'mode-converter' is used to create the desired orientation of the injected wave.

The device is equipped with various plasma diagnostics.<sup>7</sup> The Langmuir probe system consists of one single and two triple movable probes. The optical diagnostics include video diagnostics, a photo-detector, and optical emission spectroscopy. Particle diagnostics include a time-of-flight neutral particle analyzer, a residual field energy analyzer, a residual gas analyzer (quadrupole mass spectrometer), and vacuum gauges.

#### **III. LANGMUIR PROBES**

A movable triple Langmuir probe is used to measure the plasma density and temperature in the horizontal mid-plane. The cylindrical tips have a length  $\ell_p = 4$  mm, a diameter  $d_p = 0.8$  mm, and a separation of 3.5 mm between each pair of the tips. The operation of the triple probe allows determining instantaneous values of the plasma parameters.<sup>2</sup> Only a simple measuring circuit is required (Fig. 2).

This theory makes some assumptions that will be addressed later in Sec. V. We assume no gradients of the plasma potential along the three pins, temperature, and electron density. The electron energy distribution in the plasma is considered to be Maxwellian (which is disputable but is out of the scope of this work). The collecting surface of electrons and ions is initially assumed to be equal, and the errors due to the variation in the ion saturation current are neglected.

The temperature can easily be obtained by measuring the voltage  $U_1$  (Fig. 2). The equation proposed by Chen<sup>2</sup> can be simplified to  $T_e = \frac{|U_1|}{\ln{(2)}}$ .

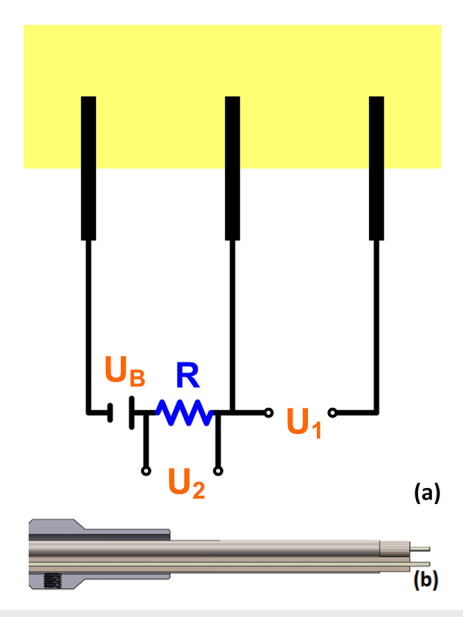


**FIG. 2.** (a) Triple probe circuit with a DC source voltage  $U_B$ , a resistor R, and voltage measurements  $U_1$  and  $U_2$  and (b) schematic view.<sup>7</sup>

The density can be calculated from the ion saturation current  $I_{sat} = q_e \cdot r_e \cdot c_s$  and the sound speed,  $c_s$ , which depends on the temperature, <sup>2</sup>

$$n_e = \frac{I_{sat}}{S_{eff} \cdot c_s \cdot e} \cdot \frac{\exp(1/2)}{\exp(\frac{e \cdot U_1}{k_B \cdot T_e} - 1)},$$
 (1)

where  $m_i$  is the ion mass,  $k_B$  is the Boltzmann constant,  $S_{eff}$  is the effective collecting area of the pin,  $U_1$  is the voltage measurement, and e and  $T_e$  are the charge and temperature of the electrons, respectively. The ion saturation current  $I_{sat}$  can be calculated using the voltage  $U_2$  over the resistance in the circuit  $I_{sat} = \frac{U_2}{R}$  with  $R = 909 \ \Omega$  (Fig. 2), and the sound speed  $c_s = \sqrt{\frac{k_B \cdot T_e}{m_i}}$ .

The effective area  $S_{eff}$  is influenced by the orientation of the magnetic field lines and the electron velocity distribution function.<sup>3</sup> In addition, sheath formation and orbital motions influence the density measurements.<sup>8</sup> It is consequently hard to get a correct value for the electron density. We will try to calibrate  $S_{eff}$  using the O-wave cut-off density.

#### IV. WAVE PROPAGATION

During the experiments, an electromagnetic wave is injected in the vessel with X-mode polarization, launched radially in the horizontal mid-plane. The absorption efficiency of this X-wave is very low (<0.02%),  $^{9,10}$  so we have to rely on multipass absorption to create a plasma. Mode conversion at reflection on the wall results in a mixture of O-mode and X-mode present in the machine. Experiments suggest a 60%–40% ratio, which means that both polarizations are present in the machine, independent of the injected polarization. The absorption efficiency for the O-wave is even 12 times lower than that for the X-wave.  $^{9,10}$ 

When the plasma density increases, a cut-off density is reached, and the X-wave cannot propagate any more in the plasma. The wave reflects back and forth between this cut-off and the Low field Side (LFS) wall and is converted to the O-wave. The absorbed power consequently decreases.

When the density increases even further, an additional mode conversion (O-X-B mode conversion) occurs when the Upper Hybrid Resonance (UHR) is reached; the O-wave is converted to the X-wave after reflection on the HFS wall and converted to the Bernstein wave at this UHR. A final conversion takes place when the O cut-off density  $n_O$  is reached. The O-wave is reflected, partly converted to X-waves and converted to the Bernstein wave. A detailed explanation of the plasma-wave interactions and conversions can be found in the Appendix.

The O cut-off density is given by

$$n_{\rm O} = \frac{\omega_{RF}^2 \cdot m_e \cdot \varepsilon_0}{e^2},\tag{2}$$

where  $\omega_{RF}$  is the frequency of the injected wave,  $m_e$  is the electron mass,  $\varepsilon_0$  is the vacuum permittivity, and e is the electron charge.

Most of the O- and X-waves in the machine are converted to Bernstein waves when this density is reached by any of the mode conversion schemes mentioned above. The coupling of this Bernstein wave is nearly 100%. Consequently there is a sudden rise in absorption, and the temperature at the position where the Bernstein wave couples will increase. This phenomenon can be used to calibrate the density measurements since it occurs at a fixed density of  $7.45 \times 10^{16} \; \text{m}^{-3}$  for an injected wave at f = 2.45 GHz.

#### V. MEASUREMENTS AND OBSERVATIONS

#### A. Experimental results

The Langmuir probe is initially positioned at the LFS wall, and a helium plasma is created with a magnetic field  $B_0 = 91.2 \text{ mT}(1600 \text{ A})$ , RF power P = 1200 W with X-mode polarization, launched radially in the horizontal mid-plane, and a pressure of  $6.35 \cdot 10^{-4}$  mbar (He gas flow = 70 SCCM). The forwarded and reflected power are measured and obtained by the Data Acquisition System (DAS). The voltages  $U_1$  and  $U_2$  (see Fig. 2) are also stored. These measurements allow calculating the density using Eq. (1), taking into account the effective surface of the probe  $S_{pr} = 2 \cdot \ell_p \cdot d_p = 6.4 \text{ mm}^2$ .

The LP is moved into the vessel, and every 0.5 cm a plasma shot is performed. This way a radial scan of the density and temperature as a function of time is obtained (Fig. 3).

It is observed that the plasma shots are reproducible:

- Plasma breakdown occurs within a 40 ms interval for the different shots, resulting in quite a smooth transition for the temperature and density measurements in the radial dimension.
- The forwarded and reflected power are quite similar for every shot (see Fig. 4).

When the R cut-off density for the X-wave  $n_R$  is reached, it cannot propagate to the ECR anymore and deposit its energy. The increase in density at the ECR seems to be stagnating (Fig. 5).

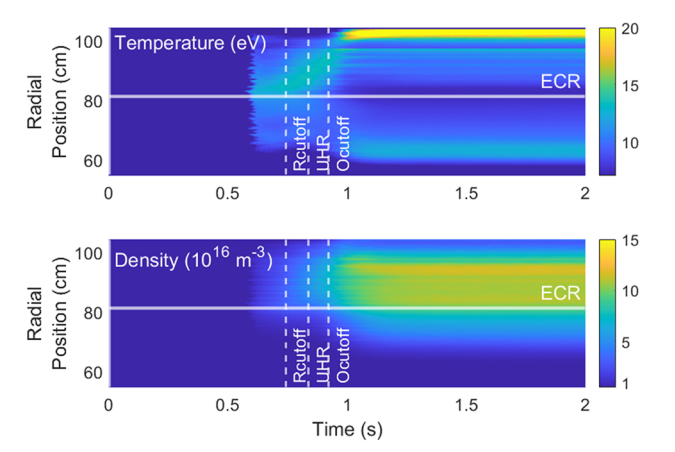


FIG. 3. Evolution of the temperature and density profile.

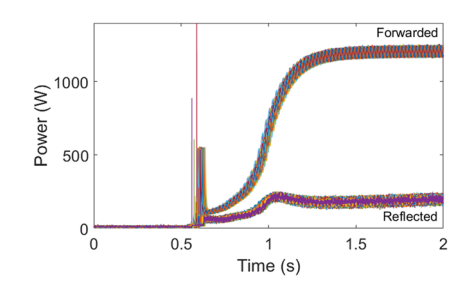


FIG. 4. Forwarded and reflected power for 1 radial scan (100 shots).

This is clearly visible in the temperature evolution at the ECR; the temperature increase abruptly ends, and a maximum is reached. The O-wave still couples at the ECR but with a much lower efficiency.

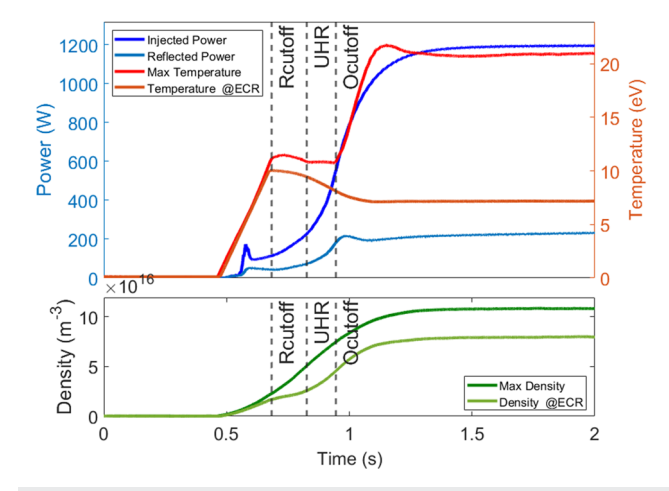


FIG. 5. Temperature and power evolution (top) and density evolution after calibration with the O cut-off (bottom).

The appearance of the UHR is also visible but harder to distinguish. A part of the X-wave is converted to the Bernstein wave, which has a 100% coupling efficiency. The density at the ECR starts to increase again while the temperature is still decreasing slightly; the power of the EBW is absorbed at the Doppler-shifted ECR between the UHR and ECR.

When the O cut-off is reached, the maximum temperature of the plasma increases again abruptly (Fig. 5). At this point, all waves are converted to the EBW by any of the mode conversion mechanisms, and the ratio of reflected to forwarded power is significantly reduced. This O cut-off density is a fixed value  $(7.45 \times 10^{16}~\text{m}^{-3})$  and can be used for calibration.

#### **B.** Calibration

We can now compare the densities measured by the triple probe [using Eq. (1)] at the O cut-off with this fixed value and determine the correction factor  $(C_{LP})$  for the Langmuir probe measurements,

$$n_e = \frac{(m_i)^{1/2} \cdot U_2}{C_{LP} \cdot S_{Pr} \cdot R} \cdot \frac{\exp(1/2)}{e(k_B T_e)^{1/2} \cdot \exp\left(\frac{e \cdot U_1}{k_B \cdot T_e} - 1\right)}.$$
 (3)

Several of these radial scans were performed to determine the influence of different parameters on the Langmuir probe measurements:

- Magnetic field: 79.8-108.3 mT (1400-1900 A).
- Injected power: 900-6000 W.
- The polarization of the injected wave (O or X).
- Gas pressure:  $5.0 6.3 \times 10^{-4}$  mbar.

It was observed that there is no influence of the injected power on the effective surface of the probe measurements. The electron temperature at the O cut-off is low and stays constant (12–13 eV) in all these cases. Although we cannot explicitly conclude that the electron energy distribution function (EEDF) is Maxwellian in these ECRH plasmas, the independence from the injected power suggests that the influence on the temperature measurements is constant and rather small

It was also observed that neither the polarization of the injected wave nor the gas pressure has an influence on the effective surface. The magnetic field, however, seems to have a large influence

#### C. Influence of the magnetic field

Several scans were performed in the TOMAS device to determine the relation between the correction factor and the applied magnetic field  $B_0$ . Figure 6 shows the effective surface  $S_{eff} = C_{LP} \cdot S_{pr}$  as a function of magnetic field  $B_0$ , with respect to the probe cross section  $S_{pr} = 2 \cdot \ell_p \cdot d_p = 6.4 \, \mathrm{mm}^2$ . A linear correlation between  $C_{LP}$  and the magnetic field  $B_0$ , and hence the position of the ECR, is observed. The variation in the effective surface is quite large, ranging from 0.2 to 2.0 times the probe cross section  $S_{pr}$ .

We can conclude that

• for a magnetic field of  $B_0 = 95.1$  mT (I = 1668 A), this correction factor is equal to 1.

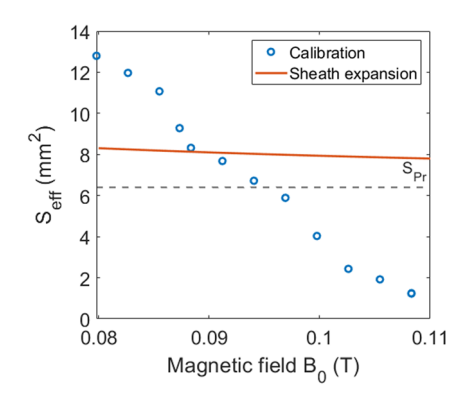


**FIG. 6.** Influence of the magnetic field on the effective probe surface as observed by the calibration and on the probe sheath expansion.

- as the magnetic field increases, and the position of the ECR is closer to the LFS, the effective surface seems to become only a fifth of the original surface (1.3 mm<sup>2</sup>).
- as the magnetic field decreases, and the position of the ECR is closer to the HFS, the effective surface seems to become slightly larger than the entire surface of the probe:  $S_{tot} = \pi \cdot \ell_p \cdot d_p + \pi \cdot \frac{d_p^2}{\ell} = 10.6 \text{ mm}^2$ .
- a calibration curve for ECRH plasma is obtained for the triple Langmuir probe in the TOMAS device for helium.
   This can be used in future experiments.

Similar behavior has been observed by Usoltceva,<sup>3</sup> where the influence of the dimensionless magnetic field strength  $\beta = \frac{r_{pr}}{r_{ce}}$  on the effective collecting surface is evaluated. The variation in this area is, however, limited to a few percent at relevant magnetic fields. This could be explained by the fact that—due to lower temperatures—the error on the density measurements due to the variation in the ion saturation current is limited, as predicted by Chen.<sup>2</sup>

To determine the error on the density measurements at larger temperatures, the probe sheath expansion can be evaluated using the work by Podolnik,<sup>4</sup> where a similar movable probe was used. The influence of the magnetic fields on the probe effective collecting area is evaluated by a 3D particle-in-cell modeling and compared using probe measurements and by lithium beam emission spectroscopy. The results of this theory that applied to our parameters are presented in Fig. 6 in orange. A deviation of up to 30% with respect to the probe surface  $S_{pr}$  is observed, as predicted by Chen<sup>2</sup> for temperatures above 10 eV. The influence of the magnetic field is not as high as that observed during the calibration experiments and is limited to 3%.

It is clear that for our case, the probe sheath expansion cannot account for the variation in the effective surface with respect to the magnetic field. Other mechanisms have to be considered. Modeling of the transport processes in the machine can perhaps help determine the cause for the variation in the effective probe surface.

#### VI. CONCLUSION

The accuracy of the density measurements of a triple Langmuir probe depends on correct determination of the effective surface, which can be hard to obtain. The O cut-off density, a fixed value for a certain frequency of the injected wave, is used for calibration of the Langmuir probe in TOMAS. It has been observed that the injected power, the polarization of the injected wave, and the pressure do not have an influence on the effective surface. The influence of the magnetic field, however, is quite large, and a linear trend is observed. The effect of probe sheath expansion alone cannot account for these variations.

A calibration curve for ECRH plasma is obtained for the triple Langmuir probe in the TOMAS device for helium, which can be used in future experiments to obtain a correct value for density measurements. A similar procedure can be used in other devices to calibrate the density measurements of a protruding Langmuir probe. Future work will include modeling of the transport processes in an attempt to determine the cause for the variation in the effective probe surface.

#### **ACKNOWLEDGMENTS**

This work has been carried out within the framework of the EUROfusion Consortium, funded by the European Union via the Euratom Research and Training Programme (Grant Agreement No 101052200—EUROfusion). Views and opinions expressed are, however, those of the author(s) only and do not necessarily reflect those of the European Union or the European Commission. Neither the European Union nor the European Commission can be held responsible for them.

#### **AUTHOR DECLARATIONS**

#### **Conflict of Interest**

The authors have no conflicts to disclose.

#### **Author Contributions**

J. Buermans: Conceptualization (lead); Formal analysis (lead); Investigation (lead); Methodology (lead); Validation (lead); Visualization (lead); Writing – original draft (lead); Writing – review & editing (lead). K. Crombé: Funding acquisition (supporting); Project administration (supporting); Supervision (equal); Writing – original draft (supporting); Writing – review & editing (equal). L. Dittrich: Writing – review & editing (supporting). A. Goriaev: Project administration (equal); Resources (equal); Writing – review & editing (supporting). Yu. Kovtun: Writing – review & editing (supporting); Writing – review & editing (supporting). S. Möller: Project administration (equal). P. Petersson: Writing – review & editing (supporting). M. Verstraeten: Software (equal); Writing – review & editing (supporting).

#### **DATA AVAILABILITY**

The data that support the findings of this study are available from the corresponding author upon reasonable request.

#### APPENDIX: WAVE PROPAGATION

As a wave propagates into a plasma, several different phenomena can occur with respect to the deposition of its wave energy: reflection, transmission, absorption, and mode conversion. An incident wave is, in general, partially reflected and partially transmitted.

- Reflection For a low field side, launching the wave sees an increase in density as it propagates toward the center. It also sees a slightly increasing magnetic field because of the 1/*R* dependence. As it reaches a zone where it cannot propagate, the wave reflects back. At this point, the perpendicular wave vector *k* → 0, and the refraction index *n* → 0; in addition, we reach a cut-off.
- **Transmission** If the evanescent region is small (with respect to the wavelength), the wave can partially tunnel through this region.
- **Absorption** A strong wave–particle resonance can occur, leading to strong absorption. This is the case where  $k \to \infty$ . The resonance occurs when the wave frequency is equal to the exact harmonic of the electron cyclotron frequency  $\omega_{ce}$ . This is called the Electron Cyclotron Resonance (ECR).
- Mode conversion This involves two different plasma waves. The incident wave encounters a wave resonance, whose mode converts it into a different type of plasma wave. For both waves, *k* → ∞ at the mode conversion location. Some of the energy of the initial wave is transferred to the second wave, which propagates further into the plasma.

The solution of the dispersion equation for the extraordinary wave (X-wave) leads to four domains: two where wave propagation is possible and two evanescent regions (Fig. 7). Three interesting values for the frequency  $\omega$  can be identified:

- **R cut-off**+ The Fast X-wave (FX) can propagate if  $\omega > \omega_R$ . For typical TOMAS parameters ( $B_0 = 91.4$  mT and f = 2.45 GHz), this leads to a cut-off density for the FX-mode starting at  $n_R = 3.30 \times 10^{15}$  m<sup>-3</sup>.
- L cut-off: The Slow X-wave (SX) can propagate if  $\omega > \omega_L$ . For typical TOMAS parameters, this leads to a cut-off density for the SX-mode starting at  $n_L = 1.52 \times 10^{17} \text{ m}^{-3}$ .
- Upper Hybrid Resonance (UHR): A wave resonance occurs for  $\omega = \omega_U$ . For typical TOMAS parameters, this starts at a density of  $n_U = 6.74 \times 10^{15} \text{ m}^{-3}$ ,

$$\omega_{R} = \frac{\omega_{ce} + \sqrt{\omega_{ce}^{2} + 4\omega_{pe}^{2}}}{2},$$

$$\omega_{L} = \frac{-\omega_{ce} + \sqrt{\omega_{ce}^{2} + 4\omega_{pe}^{2}}}{2},$$

$$\omega_{U} = \sqrt{\omega_{pe}^{2} + \omega_{ce}^{2}}.$$
(A1)

These frequencies are a function of the electron cyclotron frequency  $\omega_{ce}$  and the electron plasma frequency  $\omega_{pe}$  and depend on the magnetic field  $B_0$  and the plasma density  $n_e$ ,

$$\omega_{ce} = \frac{e \cdot B_0}{m_e}$$
 and  $\omega_{pe} = \sqrt{\frac{n_e \cdot e^2}{m_e \cdot \varepsilon_0}},$  (A2)

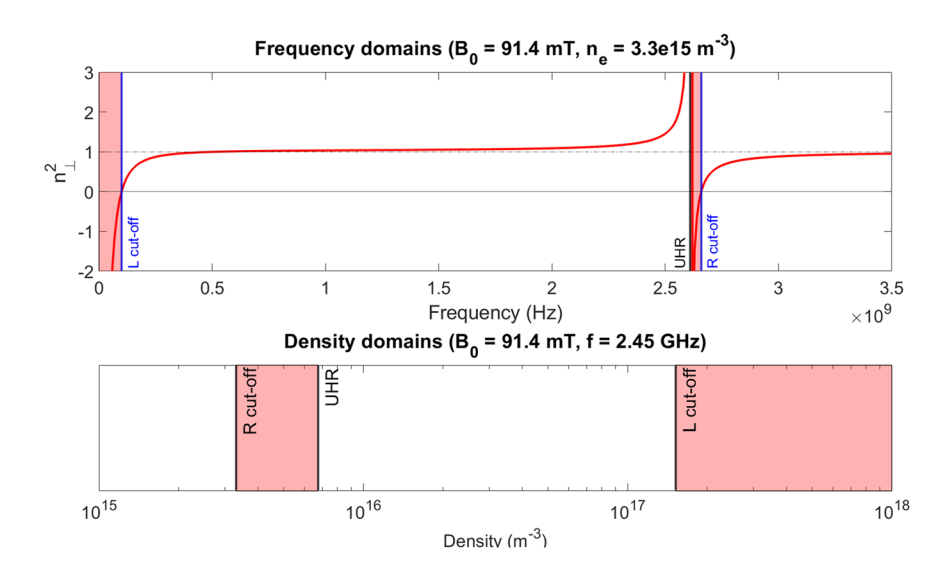


**FIG. 7.** TOMAS X-wave accessibility domains.

where  $m_e$  is the electron mass and  $\varepsilon_0$  is the vacuum permittivity.

The solution of the dispersion equation for the ordinary wave (O-wave) leads to two domains with a specific value for the frequency  $\omega$  at this interface:

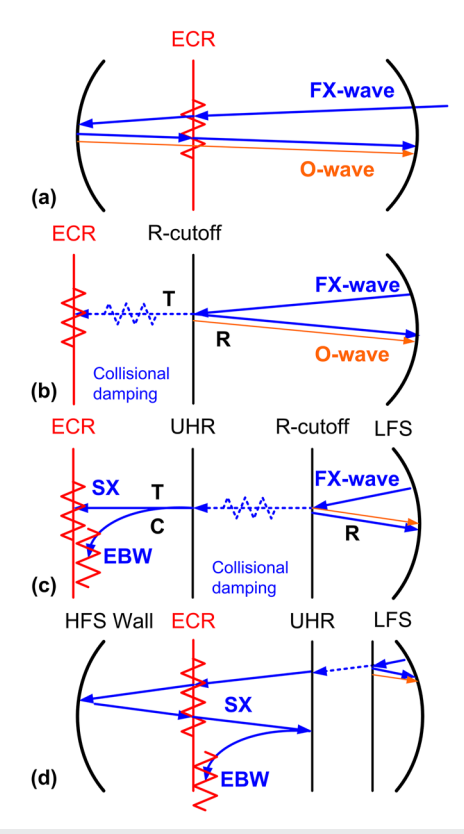


**FIG. 8.** X-wave deposition mechanisms for increasing density  $(a \rightarrow d)$ .

• **O cut-off**: The O-wave can only propagate for  $\omega > \omega_{pe}$ , which leads to a cut-off density  $n_O = \frac{\omega_{RF}^2 \cdot m_e \cdot e_0}{e^2}$ . This value only depends on the frequency  $\omega_{RF}$  of the injected wave. It thus has a value of  $7.45 \times 10^{16}$  m<sup>-3</sup> when using a 2.45 GHz magnetron for electron cyclotron heating.

The absorption efficiency of the X-wave below the R cut-off density is very low  $(<0.02\%)^{9,10}$  so we have to rely on multipass absorption to create a plasma. Mode conversion at reflection on the wall results in a mixture of O-mode and X-mode present in the machine [Figs. 8(a) and 9(a)]. Experiments suggest a 60%–40% ratio, which means that both polarizations are present in the machine,

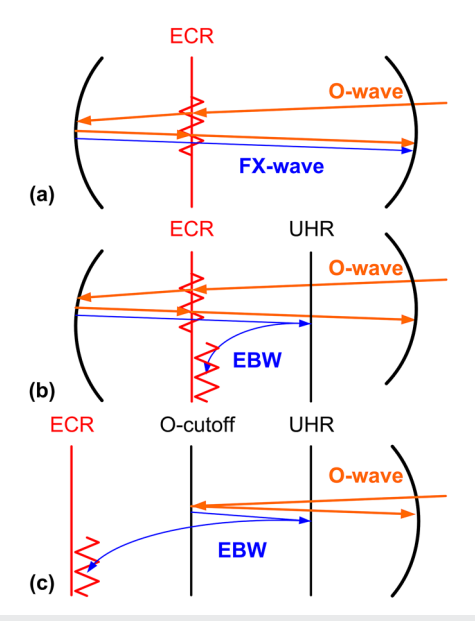


**FIG. 9.** O-wave deposition mechanisms for increasing density  $(a \rightarrow c)$ .

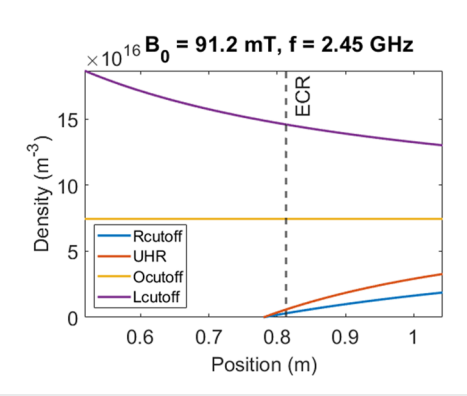


FIG. 10. Relation between position and density for cut-off densities.

independent from the injected polarization. The absorption efficiency for the O-wave is even 12 times lower than that for the X-wave.  $^{9,10}$ 

When the density increases, different deposition mechanisms are observed. When the R cut-off density  $n_R$  is reached, the X-wave cannot propagate to the ECR anymore. Only the tunneling part of the wave (T) can reach the ECR [Fig. 8(b)]. Consequently, there is a sudden decrease in absorption at this position, and the temperature decreases, while there is additional collisional damping in the evanescent region. The remainder of the wave (R) is reflected back to the Low Field Side (LFS) of the machine. A part of this reflected wave can be mode converted to the O-wave. The O-wave is not influenced by the R cut-off.

When the UHR density  $n_R$  is reached, the tunneling part (T) of the X-wave can still propagate to the ECR and deposit its energy. A part of this wave is converted (C) to the Electron Bernstein Wave (EBW) at the UHR (FX-B Mode conversion), which couples at a location close to the ECR [Fig. 8(c)]. The remainder of the tunneling part, after absorption, reflects on the High Field Side (HFS) wall and has a second pass at the resonance layer. When it reaches the UHR, it is finally converted to the EBW (SX-B Mode conversion) and returns to the HFS [Fig. 8(d)]. There is no immediate effect of the UHR on the O-wave.

The FX-B and SX-B mode conversion leads to an EBW, which has no cut-offs, but cannot propagate in vacuum since it is an electrostatic wave. The wave damps strongly (up to 100%) on electrons at the fundamental or any harmonic of the Doppler-shifted electron cyclotron resonance.<sup>11</sup>

An additional mode conversion (O-X-B Mode conversion) occurs when the O-wave is converted to the X-wave after reflection on the HFS wall and converted to the Bernstein wave at the UHR [Fig. 9(b)]. It also occurs when the O cut-off density is reached. The O-wave is reflected, partly converted to X-wave, and converted to the Bernstein wave [Fig. 9(c)].

Most of the O- and X-waves in the machine are converted to the Bernstein wave at this point by any of the mode conversion schemes mentioned above. Consequently, there is a sudden increase in absorption, and the temperature at the position where the Bernstein wave couples will increase. This phenomenon can be used to calibrate the density measurements since it occurs at a fixed density of  $7.45 \times 10^{16}~\text{m}^{-3}$ .

The densities related to this UHR and R cut-off, however, depend on the magnetic field, which is a function of the position in the device (Fig. 10). It is consequently harder to determine the exact combination of the density and position at the same time.

#### **REFERENCES**

<sup>1</sup>V. S. Mukhovatov, R. Bartiromo, D. Boucher, A. E. Costley, L. de Kock, K. Ebisawa, P. Edmonds, Y. Gribov, G. Janeschitz, L. C. Johnson, S. Kasai, E. Marmar, A. Nagashima, M. Petrov, D. E. Post, P. E. Stott, V. S. Strelkov, G. Vayakis, C. I. Walker, J. Wesley, S. Yamamoto, K. M. Young, and V. S. Zaveriaev, "Role and requirements for plasma measurements on iter," in *Diagnostics for Experimental Thermonuclear Fusion Reactors 2*, edited by P. E. Stott, G. Gorini, P. Prandoni, and E. Sindoni (Springer US, Boston, MA, 1998), pp. 25–40.

<sup>2</sup>S. L. Chen and T. Sekiguchi, "Instantaneous direct-display system of plasma parameters by means of triple probe," J. Appl. Phys. **36**, 2363–2375 (1965).

<sup>3</sup>M. Usoltceva, E. Faudot, S. Devaux, S. Heuraux, J. Ledig, G. V. Zadvitskiy, R. Ochoukov, K. Crombé, and J.-M. Noterdaeme, "Effective collecting area of a cylindrical Langmuir probe in magnetized plasma," Phys. Plasmas 25, 063518 (2018).

<sup>4</sup>A. Podolník, M. Komm, J. Adámek, P. Háček, J. Krbec, R. Dejarnac, J. P. Gunn, and R. Pánek, "3D particle-in-cell modeling of Langmuir probe effective collecting area in magnetized plasma," Plasma Phys. Controlled Fusion **60**, 085008 (2018).

<sup>5</sup>H. B. Störk, J. Winter, J. Ihde, H. G. Esser, H. Reimer, and M. Freisinger, "Tomas - a toroidal magnetized plasma facility for studying wall conditioning of future fusion devices," Fusion Technol. 39, 54–60 (2001).

<sup>6</sup>A. Goriaev, T. Wauters, S. Möller, R. Brakel, S. Brezinsek, J. Buermans, K. Crombé, A. Dinklage, R. Habrichs, D. Höschen, M. Krause, Y. Kovtun, D. López-Rodríguez, F. Louche, S. Moon, D. Nicolai, J. Thomas, R. Ragona, M. Rubel, T. Rüttgers, P. Petersson, P. Brunsell, C. Linsmeier, and M. Van Schoor, "The upgraded TOMAS device: A toroidal plasma facility for wall conditioning, plasma production, and plasma–surface interaction studies," Rev. Sci. Instrum. 92, 023506 (2021).

<sup>7</sup>Y. Kovtun, A. Goriaev, D. López-Rodríguez, L. Dittrich, P. Petersson, S. Moon, T. Wauters, K. Crombé, S. Möller, J. Buermans, M. Verstraeten, and S. Brezinsek, "Overview of TOMAS plasma diagnostics," J. Instrum. 8, C02034 (2023).

<sup>8</sup>I. B. Bernstein and I. N. Rabinowitz, "Theory of electrostatic probes in a low-density plasma," Phys. Fluids **2**, 112–121 (1959).

<sup>9</sup>M. Bornatici, R. Cano, O. De Barbieri, and F. Engelmann, "Electron cyclotron emission and absorption in fusion plasmas," Nucl. Fusion 23, 1153 (1983).

<sup>10</sup>J. Buermans, "X-mode electron cyclotron heating scenarios beyond the cutoff density," in *Proceedings of the 24th Topical Conference on Radio-frequency Power* in Plasmas, 2022.

 $^{11}$ T. Maekawa, T. Kobayashi, S. Yamaguchi, K. Yoshinaga, H. Igami, M. Uchida, H. Tanaka, M. Asakawa, and Y. Terumichi, "Doppler-shifted cyclotron absorption of electron Bernstein waves via  $n_{\parallel}$ -upshift in a tokamak plasma," Phys. Rev. Lett. **86**, 3783–3786 (2001).